Research Article

Geometrical transition properties of vortex cavitation and associated flow-choking characteristics in poppet valves

Liang LU[1,2], Zhongdong LIANG[1], Yuming LIU[1], Zhipeng WANG[2✉], Shohei RYU[3]

[1]*School of Mechanical Engineering, Tongji University, Shanghai 201804, China*
[2]*Frontiers Science Center for Intelligent Autonomous Systems, Tongji University, Shanghai 201210, China*
[3]*Technical Research Laboratory, Hitachi Construction Machinery Co. Ltd., Tsuchiura 300-0013, Japan*

Abstract: Poppet valves have become increasingly significant in ensuring precise digital flow rate and pressure control in hydraulic systems, necessitating a more profound understanding of the geometrical properties of cavitation in them, as well as associated flow-choking conditions. Through a comparative analysis with experimentally observed cavity images, we found that Large Eddy Simulation (LES) turbulence modeling effectively replicates the geometrical properties of cavitation in these valves. The analysis demonstrated that cavitation is generated from vortices that result from the interaction between the notch contracta flow and the surrounding fluid structure. Variations in the internal or external vena contracta conditions result in fixed or discrete cavities, and the length-to-diameter ratio serves as a measure of the transition between internal and external vena contracta flow properties. This study establishes a threshold length-to-diameter ratio of approximately 2 for the tested poppet valves. More specifically, in notch structures with a smaller valve opening, longer sealing length, and smaller throttling angle (corresponding to a larger length-to-diameter ratio), the liquid-to-vapor transfer process is more evident than in the reverse direction. A long-standing vapor cavity becomes fixed inside the notch, leading to a more pronounced flow-choking phenomenon. In contrast, for structures with a smaller length-to-diameter ratio, the cavitation process for discrete vapor cavities is more complete, ensuring fluid flow continuity and significantly reducing the occurrence of the flow-choking phenomenon.

Key words: Poppet valves; Vena contracta; Vortex flow; Vapor cavity; Flow-choking

1 Introduction

The poppet valve is a commonly used structure in fluid power systems, and is known for its simple and reliable control of pressure, flow rate, and flow direction. With the advent of digital control technology, the poppet valve has garnered increased attention as a crucial component for achieving high-quality flow control, particularly in the form of high-speed on-off valves, which can switch in less than 1 ms (Pan and Plummer, 2018). This new popularity is evident in its application in various systems, such as hydraulic pilot control systems for construction machinery (Wang et al., 2017) and fuel-metering systems for aero-engines (Gao et al., 2022). As technical requirements continue to evolve, research on the inherent problems of poppet structures is in progress. Chiavola (Chiavola et al., 2019) designed an experimental setup to test the influence of pressure fluctuations on the static characteristics of a poppet valve at different opening positions. Stosiak (Stosiak et al., 2023) measured the vibration of a micro relief valve with a poppet structure and proposed a modified decision-tree induction algorithm to analyze the impact of vibration on the valve. Li (Li et al., 2021) proposed a signal analysis method based on Ensemble Empirical Mode Decomposition, which allows for a comprehensive analysis of the intensity of cavitation flow in poppet valves. To obtain information on detailed flow conditions inside valve structures, computational fluid dynamics (CFD) is commonly utilized. For the turbulence model, Unsteady Reynolds-Averaged Navier-Stokes (URANS) is frequently employed to average the transient pulsating flow and process the Reynolds stress using two-equation k-ε

✉ Zhipeng WANG, wangzhipeng@tongji.edu.cn

 Liang LU, https://orcid.org/0000-0002-9403-330X
  Zhipeng WANG, https://orcid.org/0000-0003-4632-9170

models. For example, Gao et al. (Gao et al., 2019) used the k-ε model to conduct a numerical simulation of the flow field in large-flow high-speed on-off valves. The results showed that formation of vortices in the flow channel extracted energy from the main flow and enhanced fluid-borne noise. Based on the simulation results of the k-ε model, Filo et al. (Filo et al., 2021) modified the geometry of the check valve, resulting in a significant reduction in pressure loss.

Furthermore, when considering throttling cavitation in various valves, its mechanism is generally estimated using the continuity equation and Bernoulli's law (Han et al., 2017; Martelli et al., 2017; Zhang et al., 2018). The notch throttling flow creates a vena contracta where maximum velocity and minimum pressure occur at its throat. If the pressure drops below the local vapor pressure, bubble nucleation occurs, forming visible vapor cavities. The URANS k-ε turbulence model aligns well with the averaged flow-field assumption, which is now commonly coupled with multi-phase and cavitation submodels to analyze severely turbulent poppet-valve cavitation. Yuan et al. (Yuan et al., 2019) elucidated the close connection between cavitation inception and the transition of the flow pattern in poppet valves, which contributed to understanding of flow-choking problems. With the advancements in high-speed flow visualization technology, several researchers, including the authors, have observed the presence of relatively large vapor cavities in throttling devices during experiments, and proposed that their generation might be linked to local vortices (Altimira and Fuchs, 2015; Kumagai et al., 2016; Min et al., 2020). Continuing to use the URANS k-ε turbulence model would make it quite difficult to accurately replicate the real scale of the notch cavity. Building upon this foundation, the authors (Lu et al., 2020) employed Large Eddy Simulation (LES) as a substitute, which demonstrated notable advantages in replicating the shape of large vapor cavities. Yuan et al. (Yuan et al., 2019; Yuan et al., 2022) provided illustrations of the discrete cavitation-formation mechanism in poppets and discussed how variations in viscosity can lead to changes in the interaction between vortex cavitation and attached cavitation (Yuan et al., 2021). Their work reinforced the concept of vortex cavitation. However, existing research has primarily focused on line-sealing poppet-valve structure. In reality, the flow-choking phenomenon could be even more se-

vere in face-sealing valves. In this paper, we use two representative poppet valve cases, one line-sealing and the other face-sealing, to demonstrate the discrepancy between discrete and fixed vortices, along with the associated discrete and fixed vapor cavities, based on the external and internal flow vena contracta theory. A critical index of length-to-diameter ratio, constituted by notch configural parameters, is proposed to measure the state-transition process of vena contracta flow. The flow-choking phenomenon is explained from the perspective of vortex-cavitation mass transfer. Such specific delineation of poppet-valve cavitation may be helpful in furthering anti-cavitation design of valve structures.

2 Experimental Approach

2.1 Parameter design

As basic fluid mechanics theory suggests (Finnemore and Franzini, 2002), the thin-wall-orifice structural characteristic exists when the thickness (length) of a wall is very small relative to the size of the opening (diameter). In other words, when the length-to-diameter ratio of an orifice is quite small, it produces a vena contracta downstream of the orifice outlet. In contrast, the thick-wall-orifice structural characteristic is present if the length-to-diameter ratio is more than 2 or 3, resulting in a vena contracta inside the orifice. Since the vena-contracta flow velocity is significantly higher than the surrounding flow, friction shear occurs, leading to the formation of two distinct types of local vortex. For the thick-wall orifice shown in Fig. 1a, the vena contracta occurs inside the orifice, and the interaction between the expansion flow and orifice wall generates fixed vortices. In the case of the thin-wall-orifice shown in Fig. 1b, the vena contracta occurs outside the orifice. Here, the interaction between the expansion flow and surrounding fluid leads to formation of a series of discrete and traveling vortices, independent of the influence of the orifice wall.

The theoretical definition of the orifice structure in fluid mechanics could be applied to the poppet-valve situation under examination. As shown in Fig. 2, the valve opening L_x, sealing length L_s, and throttling angle α are defined. The rectangle *A-B-C-D* represents the cross-section of the annular throttling domain, which could also be considered a typical

hydrodynamic orifice structure. As mentioned above, the flow characteristics of the thin-wall and thick-wall orifices would result in significant differences in the vena contracta and related vapor conditions. To establish a reasonable measurement basis, it is first necessary to determine the length-to-diameter ratio. As shown in Fig. 2, due to the identical flow properties of all sections such as *A-B-C-D*, it is reasonable to consider *A-B-C-D* as the rotationally symmetric cross-section of a certain tapered cylindrical domain, with the length of *A-B* or *D-C* as "diameter" and the length of *A-D* or *B-C* as "length". Thus, the parameter "length-to-diameter ratio" of the 2D flow domain *A-B-C-D* could be defined as the ratio of length *A-D* to *A-B*, which can be expressed by the equation:
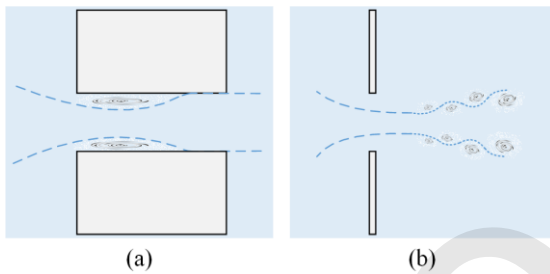
$$R_a = \frac{L_s}{L_x \sin \alpha}. \tag{1}$$

Fig. 1 Two types of flow vena contracta: (a) internal vena contracta for the thick-wall orifice; (b) external vena contracta for the thin-wall orifice

2.2 Experimental system

To observe the cavitation near the notch of the poppet valve, we designed a comprehensive visualization experiment system, as shown in Fig. 2. The pump station provided the necessary flow circulation for the test valve, with a parallel relief valve installed to modify the inlet pressure and an in-series throttling valve to adjust the outlet pressure. The flowmeter was positioned downstream of the pump to record the test flow rate, while essential accessories such as a safety valve and filter were included to ensure smooth functioning of the entire system. To conduct the test procedures, we equipped the system with a high-speed camera and two pressure gauges. The camera was capable of capturing a maximum of 600 thousand images per second, and had a xenon lamp to provide sufficient light intensity. Correspondingly, the test valve body was constructed using transparent PMMA material with a refractive index of 1.49, transmittance of 92, and haze of 1.5, to meet the visualization requirements. The pressure gauges were positioned close to the test valve inlet and outlet, taking into account the need to minimize the simulation domain. Moreover, the latter section of the poppet was designed in a threaded shape with a graduated disc at the end, allowing for precise adjustment and measurement of the throttle opening.
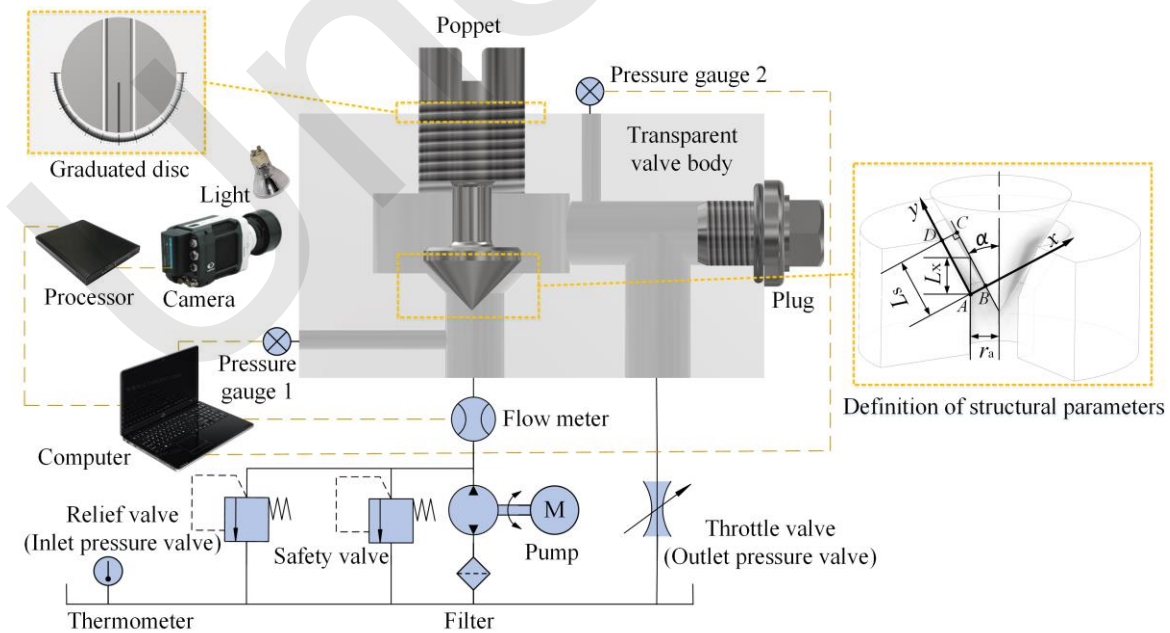

Fig. 2 Schematic of the experimental system, including definitions of structural parameters

The extent of cavitation or potential of its occurrence could be described by a dimensionless number known as the cavitation number, as shown in Eq. (2).

$$\sigma = \frac{p_{out} - p_v}{p_{in} - p_{out}}, \qquad (2)$$

where p_{in} and p_{out} represent the inlet and outlet pressure of the test poppet valve, respectively, while p_v denotes the vapor pressure under specific temperature conditions. To ensure the safety of the PMMA material, the experiment was conducted under low-pressure conditions, and the inlet pressure p_{in} was maintained constant at 3.0 MPa. As the occurrence of cavitation is not dependent on pressure but mainly related to the dimensionless cavitation number (Brennen, 2014), conducting experiments under low-pressure conditions allowed us to effectively observe the cavitation phenomenon. We used L-HM 46 hydraulic oil, a mineral oil widely used in fluid power transmission and control systems. All the experimental parameters involved in this study are listed in Table 1. Additionally, we analyzed more structural parameters through numerical calculations.

3 Experimental Approach

3.1 Experimental system

The simulation flow domain was constructed based on the test-valve structure and boundary-pressure metering conditions, corresponding to Fig. 2. Although the outlet flow channel was not perfectly circular, the 3D flow domain could be generally treated as axisymmetric. Therefore, the simulation flow domain could be simplified to a 2D cross-section, as shown in the area surrounded by thick solid lines in Fig. 3a.

As mentioned in the introduction, the LES turbulence model has demonstrated promising results in simulating cavitation generated by vortices, thus making it applicable in this study. For LES, we employed a high-quality structured grid to ensure accuracy and efficiency of calculation. Due to the limited flexibility of structural grids, a partitioned division approach was required. As shown in Fig. 3b, the

Table 1 Experimental parameters

| Physical parameters		Structural parameters		Flow parameter	
Density of liquid oil ρ_l	889 kg/m^3	Inlet radius r_a	4 mm	Inlet pressure p_{in}	3.0 MPa
Viscosity of liquid oil μ_l	0.045 kg/(m s)	Sealing length L_s	0,2,4,6 mm	Outlet pressure p_{out}	≥0.15 MPa
Density of vapor oil ρ_v	0.55 kg/m^3	Valve opening L_x	1 mm	Temperature	40 ±1 ℃
Viscosity of vapor oil μ_v	1.34×10^{-5} kg/(m s)	Throttling angle α	30 °, 45 °, 60 °		
Vapor pressure p_v	10 Pa				
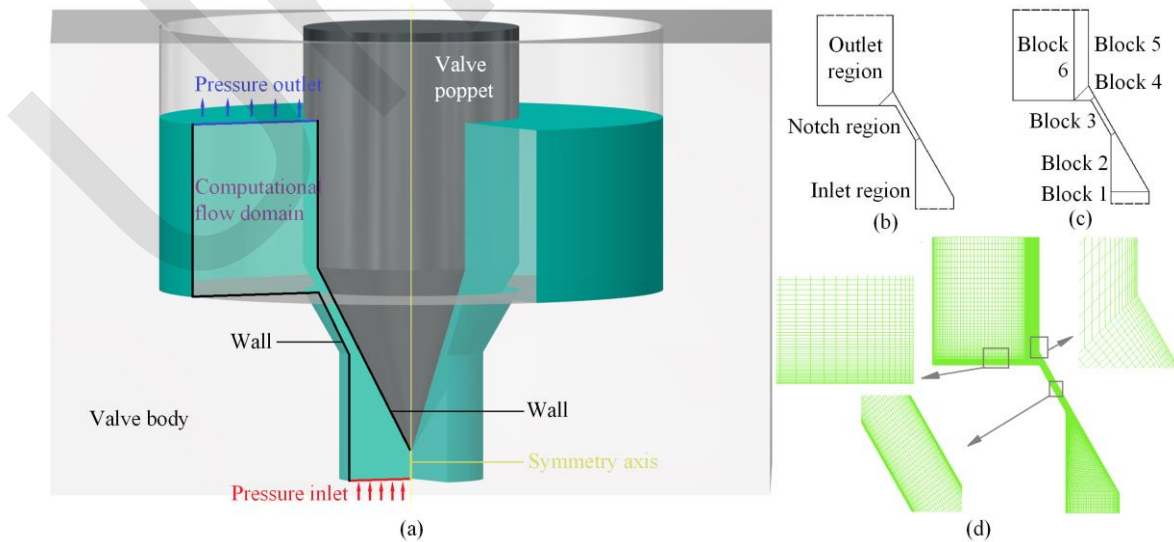
Fig. 3 Simplification and gridding of the computational fluid domain: (a) simplified computational flow domain; (b) region partition; (c) blocking; (d) gridding

computational domain consisted of the inlet region, valve-notch region, and outlet region. To ensure that each region had a quadrilateral structure, six quadrilateral blocks were further segmented, as illustrated in Fig. 3c. It is necessary to clarify that Block 3 did not exist for the line-sealing poppet valve. The near-wall area of the grid was refined, with the wall distance set at 1μm and the grid growth rate at 1.05. This ensured that the dimensionless wall distance y^+ of the grid was strictly less than 1, placing the first grid cell within the viscous sublayer. As a result, the wall shear stress could be accurately calculated directly from the velocities in the first cell without using a wall function. In addition, to thoroughly analyze the cavitation phenomenon in the notch region, block 3 and block 4 had a large number of grid nodes, as shown in Fig. 3d.

3.2 Governing equations

3.2.1 Multiphase model

In fluid power-transmission and control systems, the average sound velocity of hydraulic oil is approximately 1300 m/s, and the maximum flow velocity typically does not exceed 200 m/s. Consequently, in this study the fluid was considered to be incompressible. Assuming that the current flow is characterized by homogeneous multiphase flow with phases moving at the same velocity, the Mixture model (Manninen et al., 1996), a simplified multiphase model, can be employed:

$$\rho_{\mathrm{m}} = \rho_{\mathrm{v}}\alpha_{\mathrm{v}} + \rho_{\mathrm{l}}(1-\alpha_{\mathrm{v}}), \qquad (3)$$

$$\mu_{\mathrm{m}} = \mu_{\mathrm{v}}\alpha_{\mathrm{v}} + \mu_{\mathrm{l}}(1-\alpha_{\mathrm{v}}), \qquad (4)$$

where α_{v} represents the volume fraction number of vapor, ρ_{m}, ρ_{l}, and ρ_{v} are the density of the mixture, liquid, and vapor, respectively, and μ_{m}, μ_{l}, and μ_{v} are the dynamic viscosity of the mixture, liquid, and vapor, respectively.

3.2.2 Turbulence model

Generally, turbulence is characterized by vortices with a wide range of lengths and time scales. Implicit LES resolves large energy-containing eddies at grid nodes, while smaller, isotropic eddies are handled by the sub-grid scale turbulence model to close the governing equations. The LES equations are derived by applying a second-order commuting filter

to the incompressible Navier–Stokes equation and continuity equation (Ghosal and Moin, 1995):

$$\frac{\partial \rho_{\mathrm{m}}}{\partial t} + \frac{\partial \left(\rho_{\mathrm{m}}\bar{u}_j \right)}{\partial x_j} = 0, \qquad (5)$$

$$\frac{\partial \left(\rho_{\mathrm{m}}\bar{u}_i \right)}{\partial t} + \frac{\partial \left(\rho_{\mathrm{m}}\bar{u}_i\bar{u}_j \right)}{\partial x_j} = -\frac{\partial \bar{p}}{\partial x_j} + \frac{\partial}{\partial x_j}\left(\mu_{\mathrm{m}} \frac{\partial \bar{u}_i}{\partial x_j} \right) - \frac{\partial \tau_{ij}}{\partial x_j}, \quad (6)$$

where t is the time, p is the pressure, u is the velocity, and τ_{ij} denotes the sub-grid scale stresses (SGS). The complete form of the momentum equations for 2D axisymmetric geometries are listed in the electronic supplementary material (ESM) S1.

The Boussinesq hypothesis (Hinze, 1975) was employed to model the SGS tensor, which was generated by the filtering operation in LES:

$$\tau_{ij} = -2\mu_{\mathrm{t}}\bar{S}_{ij}, \qquad (7)$$

where μ_{t} represents the eddy viscosity and $\bar{S}_{ij}$ denotes the rate-of-strain tensor for the resolved scale. It should be noted that the SGS tensor also contained isotropic components, which were added to the filtered static pressure term without the need for additional modeling. We used the Wall-Adapting Local Eddy Viscosity (WALE) model (Nicoud and Ducros, 1999) to further model the eddy viscosity, and its complete formulas are provided in the ESM S2.

3.2.3 Cavitation model

Cavitation models suggests that cavitation is formed by the development of nuclei bubbles in the low-pressure zone of the liquid. We used the models to simulate the process of liquid evaporating under lower local pressure and condensing under greater local pressure, in comparison to the vapor pressure at the local temperature. Common cavitation models include the Full Cavitation model (Singhal et al., 2002), the Schnerr-Sauer model (Schnerr and Sauer, 2001), and the Zwart-Gerber-Belamri model (Zwart et al., 2004). The Full Cavitation model considers all first-order effects, including non-condensable bubbles, bubble dynamics, phase transitions, and turbulent pressure fluctuations. However, it is numerically unstable and cannot be coupled with the LES. The remaining two models differ significantly from the first; they are robust and converge quickly. The

Schnerr-Sauer model (Schnerr and Sauer, 2001) uses vapor volume fraction for two-phase modeling; this closely corresponds to our grayscale experimental vapor images, making it the preferred choice for this study:

$$\frac{\partial\left(\rho_{v}\alpha_{v}\right)}{\partial t} + \frac{\partial\left(\rho_{v}\alpha_{v}u_{j}\right)}{\partial x_{j}} = \dot{m}^{+} - \dot{m}^{-}, \qquad (8)$$

where the source term $\dot{m}^{+}$ represents evaporation and $\dot{m}^{-}$ represents condensation. The complete formulas of the Schnerr-Sauer model are provided in the ESM S3.

3.3 Numerical solution

To achieve more accurate numerical results, we adopted the coupled calculation method, which requires sacrificing some computational time and CPU resources. The actual calculations were conducted using Ansys Fluent, and the detailed solution methods can be found in the ESM S4.

The physical parameters for the numerical calculations were kept identical to those in the experiment. Pressure inlet and pressure outlet were used as boundary conditions. The inlet pressure remained constant at 3.0 MPa, while the outlet pressure varied based on specific operating conditions. To approximate the unsteadiness of cavitation, we used transient calculation, with a time step size set to 10^{-6} s, and each case contained more than 4000 time steps. The calculation was considered to have converged when the residuals of velocities were below 10^{-6} and the residual of the vapor volume fraction was below 10^{-4}.

For grid independence verification, we generated a series of grids with increasing cell numbers, denoted as Grid 1, Grid 2, and Grid 3. The Grid Convergence Index (GCI), based on generalized Richardson extrapolation (Roache, 1998), was used to estimate the grid convergence of the solution and provide an error band. The complete grid refinement method and GCI calculation formulas are listed in the ESM S5. The time-averaged flow rates under the same pressure and notch-structure conditions were used as the characterization index for grid-independence verification. As shown in Table 2, further refining the grid based on Grid 2 only resulted in a maximum 0.32% change in solutions. In other words, using Grid 2 for the calculations introduced a

maximum error of 0.32%, and it was not necessary to continue refining the grid. Ultimately, we chose to use grids with identical spacing to Grid 2 for the calculations in this study.

Table 2 GCI of 3 grid conditions (L_s=4 mm, L_x=0.50 mm, α=30 °, p_{out}=0.2MPa).

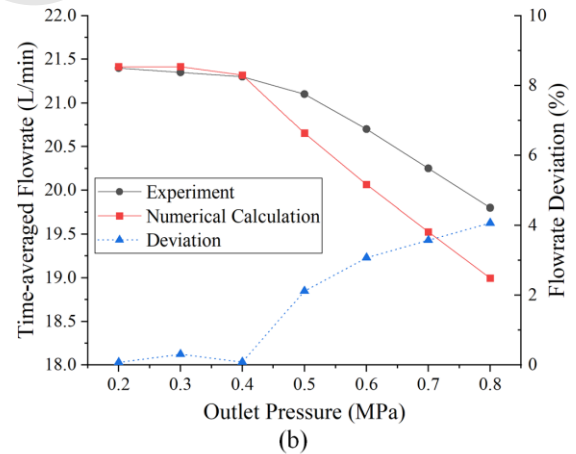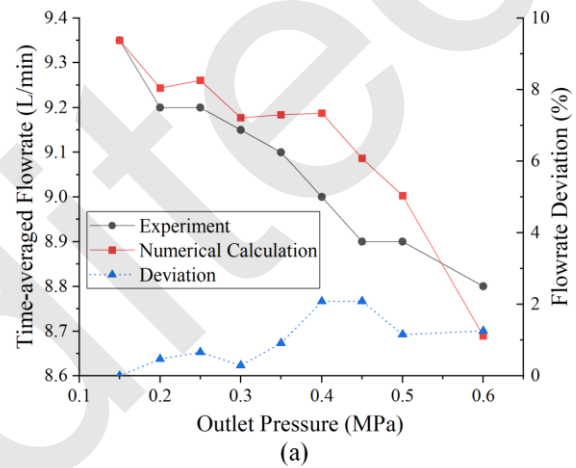|	Cell number (million)	Time-averaged flow rate (L/min)	GCI (%)
Grid 1	0.075	21.7187	2.06
Grid 2	0.3	21.4160	0.32
Grid 3	1.2	21.3687	0.05

(a)

(b)

Fig. 4 Comparison between the experimental and numerical time-averaged flow rates: (a) line-sealing (L_s=0mm, L_x=0.25mm, α=30 °, p_{out}=0.2 MPa); (b) face-sealing (L_s=4mm, L_x=0.5mm, α=30 °, p_{out}=0.2 MPa)

4 Results and Discussion

4.1 Mechanism analysis of flow-vortex-produced vapor cavities

Using two typical structures as examples (face-sealing and line-sealing poppet valves), we will discuss two distinct causes of cavitation. We must point out that two-phase flow is assumed to be homogeneous in the mixture model. Consequently, an independent vapor cavity with a clear vapor-liquid interface cannot be explicitly presented using the proposed modeling approach; a vapor fraction number of 0.6 is utilized as the isosurface threshold to divide the vapor fraction gradient into two directions (marked with different colors), allowing for a better revelation of cavitation geometry. Fig. 5 illustrates the detailed formation mechanism of the fixed vapor cavity that occurs in the face-sealing poppet valve. As shown in Figs. 5a and 5b, under the proposed conditions, the notch cavitation exhibits a fixed vapor cavity near the valve seat wall, while a few scattered vapor cavities appear downstream. The region with lower pressure than vapor pressure is concentrated in the same area, as indicated in Fig. 5c. This local low pressure appears to be generated by local vortices formed by the interaction of the internal flow vena contracta and the valve seat wall, as evident from the flow streamline distributions displayed in Figs. 5d and 5e. In comparison to Fig. 1a, one can see that the internal flow vena contracta only occurs near the valve seat under the proposed conditions, as there is no sharp edge present on the poppet side. Moreover, the essence of the cavitation process lies in the transform between the two phases. As shown in Fig. 5f, near the notch inlet, the liquid phase transforms into the vapor phase, while near the notch outlet, the vapor phase transforms back into the liquid phase. The process of liquid-to-vapor transfer is more dominant, resulting in the persistence of a fixed vapor cavity inside the notch.

Fig. 6 illustrates geometrical properties of the cavity with increasing outlet pressure (from a certain low level), with the inlet pressure maintained at 3.0 MPa and the same face-sealing poppet-valve conditions. It is clear that the cavity region consistently corresponds to the vortex region. As the outlet pressure increases, the notch flow velocity decreases, leading to a gradual reduction in the cavity scale, while the fixed shape of the cavity remains unchanged.

Regarding the line-sealing poppet valve, Fig. 7 illustrates the detailed formation mechanism of the discrete vapor cavities. As shown in Figs. 7a and 7b,

the discrete vapor cavities are distributed downstream of the notch, with hardly any fixed vapor cavity appearing. The region of lower pressure than vapor pressure is distributed downstream of the notch, as indicated in Fig. 7c. This phenomenon deviates from traditional interpretations of cavitating bubble flow that adhere to Bernoulli's law and the continuity equation. As shown in Figs. 7d and 7e, discrete vapor cavities do not occur inside the throat of the vena contracta, which is expected to have the lowest pressure and maximum flow speed. Instead, these discrete vapor cavities appear in the submerged jet-shear vortices formed by the interaction between the high-speed external vena contracta flow and the relatively static surrounding fluid. Correspondingly, the mass transfer processes occur at the same time in the shearing vortex regions. In each vortex core, the liquid phase transfers to the vapor phase, while at the edge of the vortex, the vapor phase transfers back to the liquid phase, as shown in Fig. 7f.

Fig. 8 illustrates the geometrical properties of the cavities with increasing outlet pressure (from a certain low level) with the inlet pressure maintained at 3.0 MPa under the set line-sealing poppet valve conditions. It is evident that the discreteness of the vapor cavities remains consistent with different outlet pressures, and no fixed cavity exists. As the outlet pressure decreases, the number and scale of cavities increase, and individual vapor cavities even merge into vapor clusters.
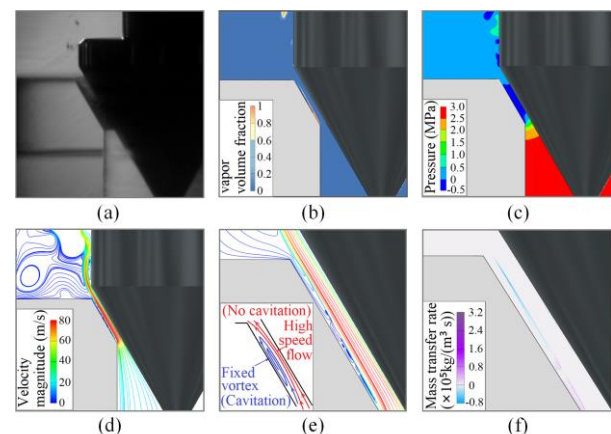

Fig. 5 Illustration of the formation of the fixed vapor cavity in a face-sealing poppet valve: (a) cavity image from experiment; (b) simulation result for cavity isosurface; (c) notch pressure distribution; (d) notch streamline distribution; (e) fixed vortex generated by internal flow vena contracta; (f) cavitation mass transfer (L_s=4 mm, L_x=1 mm, α=30 °, p_{out}=0.2 MPa)

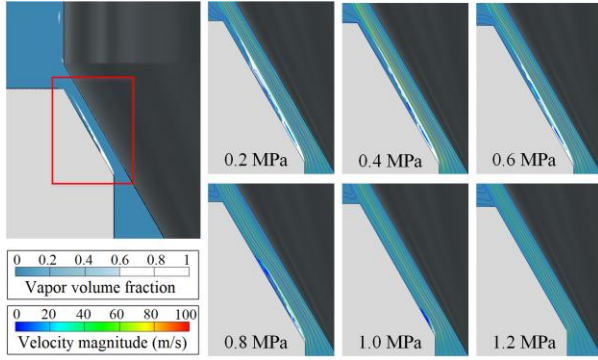**Fig. 6 Geometrical properties of the cavity with increasing outlet pressure in a face-sealing poppet valve (L_s=4 mm, L_x=1 mm, α=30 °)**
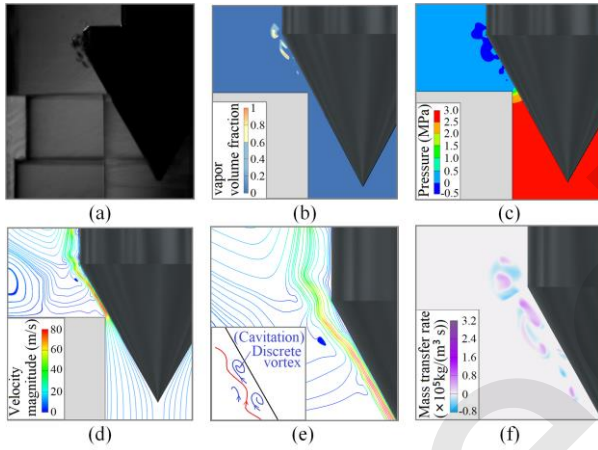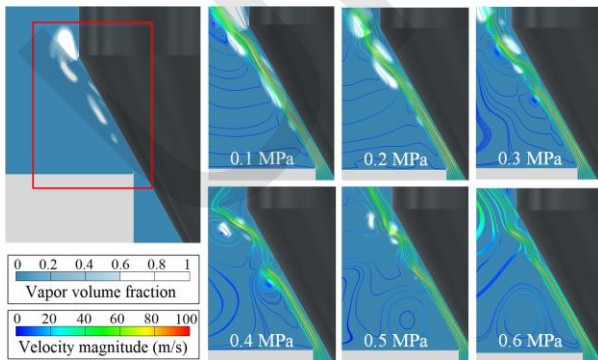

Fig. 7 Illustration of the formation of discrete vapor cavities in face-sealing poppet valve: (a) cavity image from experiment; (b) simulation result for cavity isosurface; (c) notch pressure distribution; (d) notch streamline distribution; (e) discrete vortex generated by internal flow vena contracta; (f) cavitation mass transfer (L_s=0 mm, L_x=0.5 mm, α=30 °, p_{out}=0.2 MPa)

Fig. 8 Geometrical properties of the cavities with increasing outlet pressure in a line-sealing poppet valve (L_s=0 mm, L_x=1 mm, α=30 °)

It can be concluded that both the fixed vapor cavities produced in face-sealing poppet valves and the discrete vapor cavities produced in line-sealing poppet valves are formed by flow vortices. The difference in physical properties between the internal vena contracta of the face-sealing orifice structure and the external vena contracta of the line-sealing orifice structure leads to distinct shape and distribution features of cavitation in these two patterns. Additionally, altering the pressure only changes the cavity scale, not the shape or distribution features.

4.2 Effects of the vena contracta on cavity features

The properties of the vena contracta significantly influence the properties of cavitation. The length-to-diameter ratio (R_a) serves as a reflection of the vena contracta properties, making it easier to identify the parameters that play a significant role in notch cavitation, as shown in Eq. (1). It should be noted that cavitation is a transient process. However, in this section, the primary focus is on the types of cavitation in various structures, while the transient behavior of cavitation is analyzed later. To accurately identify cavitation types, the figure showing the time step with the largest fixed cavity scale at the valve notch was selected, as shown in Figs. 9-11. For the cases without a fixed cavity at the valve notch, the figure showing the time step with the most vapor cavities was selected.

(1) Sealing length L_s

The transition of cavity geometrical properties with changes in the sealing length under representative pressure conditions is shown in Fig. 9; the valve opening and throttle angle are constant. One can see that when the sealing length is equal to or less than 1 mm, no fixed cavity appears near the valve seat, but discrete vapor cavities are present downstream. As the sealing length slightly increases, for example, at 1.25 mm, a minor but distinct fixed cavity occurs near the seat wall. With further increases in the sealing length, the fixed cavity scale becomes larger. This could be explained by the fact that as the sealing length increases, R_a increases, making the poppet notch more similar to a thick-wall orifice. This structure creates an internal vena contracta and generates fixed vortices and a fixed vapor cavity.

(2) Valve opening L_x

The transition of cavity geometrical properties with changes in the valve opening under representative pressure conditions is shown in Fig. 10. It can be observed that when the opening is less than 2 mm, a fixed cavity exists near the valve-seat wall. As the valve opening increases, the fixed cavity tends to move away from the wall. When the opening increases to nearly 2 mm, discrete vapor cavities gradually appear behind the fixed cavity. Once the opening reaches 2 mm, no fixed cavity exists and only discrete vapor cavities are present. The underlying mechanism remains the same. As the valve opening increases, R_a drops, making the poppet notch more similar to a thin-wall orifice. This structure creates an external vena contracta and generates discrete vortices and vapor cavities.

(3) Throttle angle α

Fig. 11a shows the transition of cavity geometrical properties with changes in the throttling angle under representative pressure conditions. It is clear that when the throttling angle is between 30 ° and 90 °, a fixed cavity exists near the valve seat wall. As the throttling angle approaches 90 °, the area of the fixed cavity that nearly touches the valve seat decreases, and more discrete vapor cavities appear downstream. Once the throttling angle reaches 90 °, no fixed cavity exists and only discrete vapor cavities are present. The turning point from a fixed to a discrete cavity occurs at the extreme angle of 90 °. To provide further evidence, an additional case with a different sealing length is illustrated in Fig. 11b. In this case, a similar transition process occurs, with the cavity geometrical property changing point at an angle of 48 °. The underlying mechanism remains the same. As the throttling angle increases, R_a drops, making the poppet notch more similar to a thin-wall orifice. This structure creates an external vena contracta and generates discrete vortices and vapor cavities.
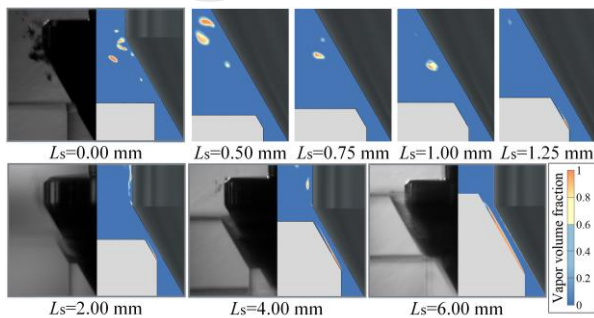

Fig. 9 Geometrical properties of the cavity with changing sealing length (L_x=1 mm, α=30 °, p_{out}=0.2 MPa)
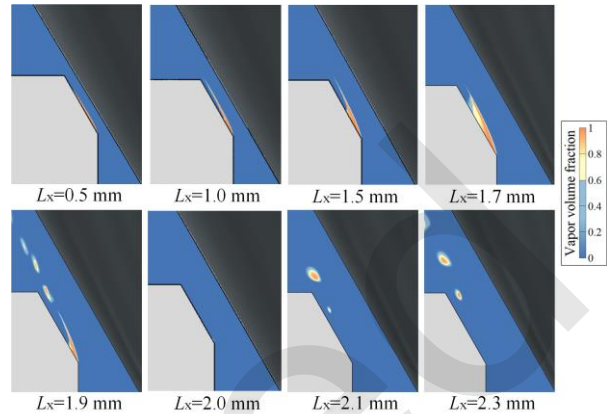

Fig. 10 Geometrical properties of the cavity as the opening changes (L_s=2 mm, α=30 °, p_{out}=0.2 MPa)
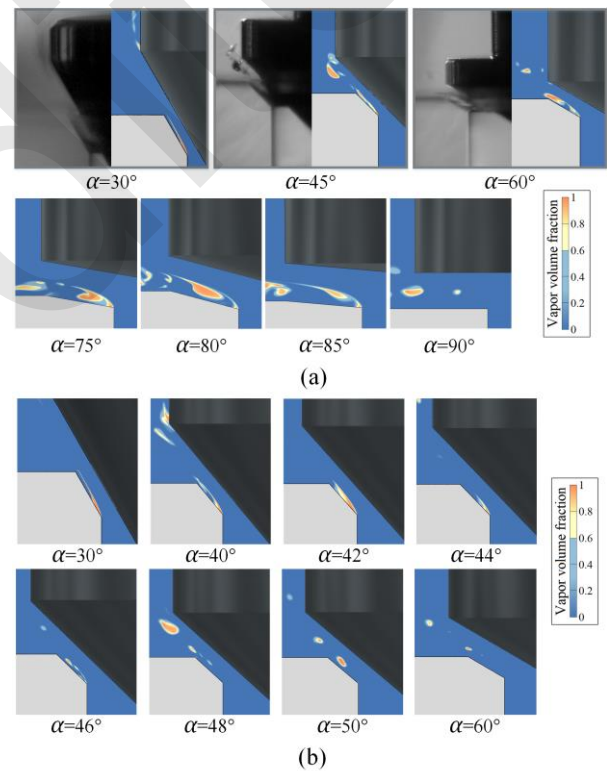

(a)

(b)

Fig. 11 Geometrical properties of the cavity as the throttling angle changes (L_x=1 mm, p_{out}=0.2 MPa): (a) with sealing length L_s=2 mm; (b) with sealing length L_s=1.5 mm

Based on the above discussion, it can be deduced that a specific R_a exists to differentiate between thick-wall-orifice and thin-wall-orifice structures and internal and external vena contracta flow conditions, as well as the geometrical properties of the fixed cavity and discrete vapor cavities. The estimated R_a

thresholds shown in Figs. 9-11 are summarized in Table 3. It is evident that the R_a thresholds are nearly the same (approximately 2) which aligns well with classical flow dynamic theory.

Table 3 Estimative of length-to-diameter ratio thresholds.

Independent variable	Sealing length L_s (mm)	Valve opening L_x (mm)	Throttling angle α (°)	Thresholds of R_a
L_s	1	1	30	2.00
L_x	2	2	30	2.00
α	2	1	90	2.00
	1.5	1	48	2.02

Further, we can calculate the absolute value of partial derivatives of R_a with respect to each of the three parameters (L_s, L_x, and α) in Eq. (1):

$$\begin{cases} \left|\dfrac{\partial R_a}{\partial L_s}\right| = \dfrac{1}{L_x \sin \alpha} = \dfrac{R_a}{L_s} \\ \left|\dfrac{\partial R_a}{\partial L_x}\right| = \dfrac{L_s}{L_x^2 \sin \alpha} = \dfrac{R_a}{L_x} \\ \left|\dfrac{\partial R_a}{\partial \alpha}\right| = \dfrac{L_s \cos \alpha}{L_x \sin^2 \alpha} = \dfrac{R_a}{\tan \alpha} \end{cases} \quad . \quad (9)$$

Here, when L_s is equal to L_x, equal amplitude changes in L_s and L_x have a similar effect on R_a. When L_s is not equal to L_x, changing the smaller of the two parameters is more efficient in influencing R_a. Additionally, when α is relatively small, for example $\alpha=30°$ ($\tan\alpha=0.577$), changing α can effectively alter R_a. However, $\tan\alpha$ increases sharply as α increases. When $\alpha=90°$, $\tan\alpha$ approaches positive infinity, and the rate of change of R_a with respect to α approaches zero. In other words, changing α is only effective if α is relatively small. To eliminate the fixed vapor cavity and to relieve flow-chocking, R_a should be decreased. In engineering applications, the valve opening is closely related to the flow rate and generally cannot be changed. Therefore, when the throttling angle is relatively small, it can be increased to achieve the desired effect. In other cases, it would be preferable to reduce the sealing length.

4.3 Specific explanations for flow choking involving vapor-cavity formation

The flow-choking phenomenon in control valves is widely recognized in various industrial applications (Tamburrano et al., 2019; Iravani and Toghraie, 2020; Hao et al., 2022). The early consensus from an industrial perspective is that when flow choking occurs, the pressure at the valve orifice throat can be regarded as the vapor pressure or even as zero (for hydraulic oil situations). Consequently, the flow-rate formula can still be derived from the continuity equation and Bernoulli's law, considering only the flow section from the orifice inlet to the throat. Lu et al. proposed a revised flow-rate formula based on statistics (Lu et al., 2009). However, most related research is based on parametric statistics. The insights into cavity geometrical properties in this study could provide additional information about cavitation-induced flow choking.

Fig. 12 displays the transient process of cavitation in a face-sealing poppet-valve notch. The cavity scale expands and shrinks along the length direction while remaining fixed at notch and not tending to collapse. This expansion and shrinking process might be attributable to the cavitation surge phenomenon, as discussed in our previous research on spool-valve cavitation (Lu et al., 2020). It is worth noting that the fixed cavity can persists all the time, which may be due to the stronger mass-transfer process from liquid to vapor, as shown in Fig. 5f. Since the cavity scale increases with the inlet and outlet pressure difference, as shown in Fig. 6, the effective flow area in the notch is reduced, thereby partly offsetting the increasing effect of the pressure difference on the flow rate. The process may reach a balance (Lu et al., 2022), resulting in the time-averaged flow rate hardly changing with increasing pressure difference, which leads to flow choking.

Fig. 13 shows the transient process of cavitation in the line-sealing poppet-valve notch. No fixed cavity is visible, but some individual traveling vapor cavities are traced going through a complete cavitation process, starting from inception and ending in collapse. The two-phase mass transfer is continuous throughout the process. In these conditions, the flow continuity is not broken, and the single-phase flow-rate equation remains applicable. Therefore, it can be inferred that the flow-choking phenomenon would not be obvious in line-sealing poppet valves. More specifically, it would not be obvious in poppet-valve notches with thin-walled orifices.

As mentioned above, the flow-choking phe-

nomenon is closely related to the geometrical features of the poppet-valve notch. Since R_a is proven to be suitable for measuring cavity geometrical features and the transition of the vena contracta type, it could also serve as a good indicator of the extent of flow choking. The relationships between the time-averaged flow rate and the square root of the pressure difference, with different sealing lengths, valve openings, and throttle angles, are presented in Fig. 14. It is not difficult to conclude that when R_a is quite small, the flow-rate curves are almost straight. As R_a increases, a turning point appears on the flow rate curve, and after the turning point, the curve becomes horizontal, indicating flow choking. Specifically, a larger R_a value leads to an earlier turning point, representing more severe flow choking.
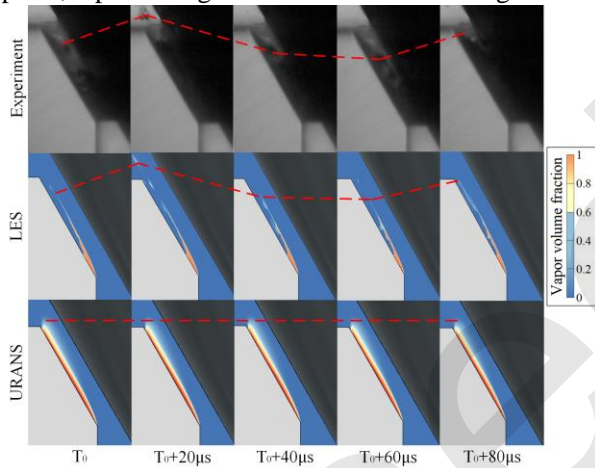

Fig. 12 Transient process of cavitation in a face-sealing poppet-valve notch (L_s=4 mm, L_x=1.5 mm, $α$=30 °, p_{out}=0.2 MPa)
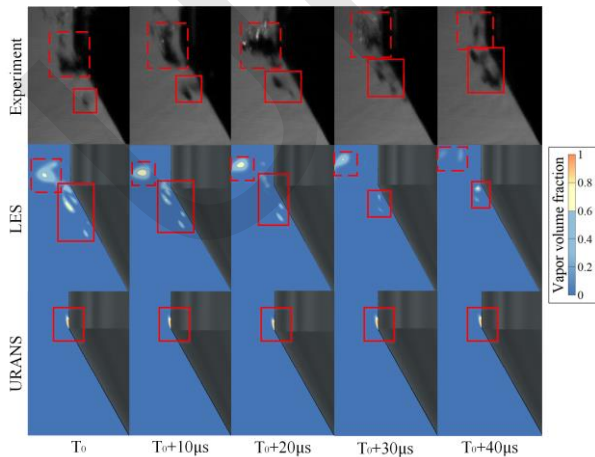

Fig. 13 Transient process of cavitation in a line-sealing poppet valve notch (L_s=0 mm, L_x=0.5 mm, $α$=30 °, p_{out}=0.2 MPa)
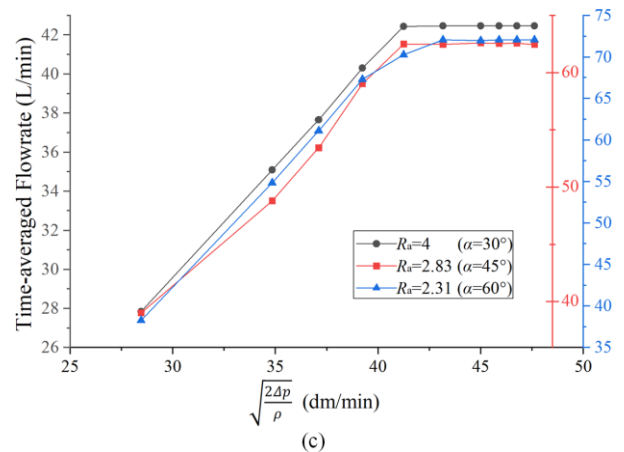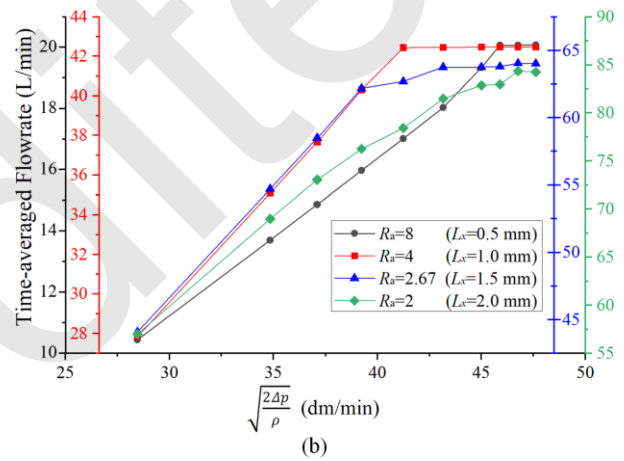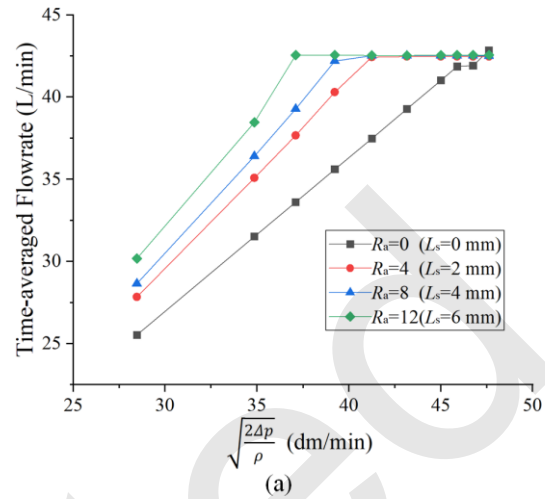

Fig. 14 Time-averaged flow rate versus the square root of the pressure difference under different R_a conditions: (a) with different sealing lengths (L_x=1.0 mm, $α$=30 °); (b) with different valve openings (L_s=2 mm, $α$=30 °); (c) with different throttle angles (L_s=2 mm, L_x=1.0 mm)

4.4 Further Explanation of the Numerical Model

To demonstrate the superior effectiveness of the LES model over the URANS model, we conducted a comparison of the notch cavitation geometry between the experimental images and the numerical results from the LES and URANS (k-ε) models. As shown in Fig. 12, the results obtained from LES successfully replicated the scale surging of the fixed vapor cavity, and the variation pattern of the vapor cavity scale for each cycle aligned closely with the experimental results. As shown in Fig. 13, although complete consistency between the LES results and the experimental results was hindered by the randomness in the formation of discrete cavities, it still effectively replicated the entire cycle of discrete cavities from inception to collapse. Regarding the URANS results, although they were derived from transient calculations, the vapor cavity geometry in each time step remained essentially unchanged, resulting in a failure to replicate the dynamic process of cavitation. For the face-sealing structure, the URANS results could only give the approximate cavitation range and could not replicate the geometrical details of the fixed cavity. In the line-sealing structure, the discrete cavities could not be replicated.

In this study, LES was applied to an axisymmetric 2D model which was designed for 3D calculation. The main consideration was to reduce the computational cost. Regarding alternative models that also reduce computational cost, as mentioned above, URANS cannot accurately replicate the cavitation at the poppet-valve notch. Although hybrid RANS-LES models can reduce the grid cell numbers on the 2D cross-section by 3-4 times for the proposed structure, because the constraints of increased resolution near the wall can be relaxed, applying these models to a 3D structure will result in overall grid cell numbers increasing by more than 10 times for such a structure. Therefore, the calculation cost would not be reduced. In this study, the geometric structure is rotationally symmetrical, and there is no significant circumferential flow. The 2D LES provides results that are very consistent with the experimental data, making it the best choice in terms of the cost-benefit measure. In fact, for certain structures under certain conditions, 2D LES can provide physically plausible results when compared with experimental results (Roohi et al., 2013; Nourazar and Safavi, 2017; Huo et al., 2021).

5 Conclusions

In this study, we investigated the geometrical properties of the vapor cavity in the poppet-valve notch and the associated flow-choking phenomenon, using visualization experiments and LES numerical approaches. Two representative cases (face-sealing and line-sealing poppet valves) are used as examples to explain the formation of vortex-produced vapor cavities. In the face-sealing poppet valve, the internal vena contracta in the notch produces fixed local vortices and a fixed large-scale vapor cavity. In the line-sealing poppet valve, the external vena contracta downstream of the notch produces discrete vortices and discrete vapor cavities. We found that the distribution of vapor cavities is associated with the local low pressure caused by vortices, which differs significantly from the traditional perspective that the cavitation process always occurs at the throat of the notch with the highest velocity.

We also found that the properties of the vena contracta and vapor-cavity geometry are determined by notch structure. The pressure condition only affects the number or scale of vapor cavities. The length-to-diameter ratio (R_a) is determined by the valve opening, sealing length, and throttling angle, which are defined to measure the transition between internal and external vena contracta flow. For structures with larger R_a, the internal vena contracta dominates, leading to a stronger mass-transfer process from liquid to vapor in the fixed cavity and resulting in significant flow choking. For structures with smaller R_a, the external vena contracta dominates, leading to a complete cavitation process in discrete vapor cavities and reducing flow choking. The R_a threshold is estimated to be approximately 2.

Author contributions

Liang LU: Conceptualization, Writing - review & editing, Supervision. Zhong-dong LIANG: Methodology, Writing -

original draft, Writing - review & editing, Formal analysis, Investigation. Yu-ming LIU: Formal analysis, Investigation. Zhi-peng WANG: Supervision. Shohei RYU: Resources.

Conflict of interest

Liang LU, Zhong-dong LIANG, Yu-ming LIU, Zhi-peng WANG and Shohei RYU declare that they have no conflict of interest.

References

Altimira M and Fuchs L, 2015. Numerical investigation of throttle flow under cavitating conditions. *International Journal of Multiphase Flow*, 75:124-136.
https://doi.org/10.1016/j.ijmultiphaseflow.2015.05.006

Brennen CE, 2014. Cavitation and bubble dynamics. Cambridge university press, Cambridge, UK, p.10-22.

Chiavola O, Frattini E, Palmieri F, Possenti G, 2019. Poppet valve performance under cavitating conditions. 74th ATI National Congress: Energy Conversion: Research, Innovation and Development for Industry and Territories, pp.020045.
https://doi.org/10.1063/1.5138778

Filo G, Lisowski E and Rajda J, 2021. Design and flow analysis of an adjustable check valve by means of CFD method. *Energies*, 14(8):2237.
https://doi.org/10.3390/en14082237

Finnemore EJ and Franzini JB, 2002. Fluid mechanics with engineering applications. McGraw-Hill Education, New York, USA, p.505.

Gao Q, Zhu YC, Chen XM and Bruno NW, 2019. CFD Simulation on Flow Field of a Large Flow Rate High Speed On/off Valve. 2019 IEEE 8th International Conference on Fluid Power and Mechatronics (FPM), pp.224-230.
https://doi.org/10.1109/FPM45753.2019.9035785

Gao Q, Zhu Y and Liu JH, 2022. Dynamics modelling and control of a novel fuel metering valve actuated by two binary-coded digital valve arrays. *Machines*, 10(1):55.
https://doi.org/10.3390/machines10010055

Ghosal S and Moin P, 1995. The basic equations for the large eddy simulation of turbulent flows in complex geometry. *Journal of Computational Physics*, 118(1):24-37.
https://doi.org/10.1006/jcph.1995.1077

Han MX, Liu YS, Wu DF, Zhao XF and Tan HJ, 2017. A numerical investigation in characteristics of flow force under cavitation state inside the water hydraulic poppet valves. *International Journal of Heat and Mass Transfer*, 111:1-16.
https://doi.org/10.1016/j.ijheatmasstransfer.2017.03.100

Hao QH, Wu WR and Tian GT, 2022. Study on reducing both flow force and cavitation in poppet valves. *Proceedings of the Institution of Mechanical Engineers Part C: Journal of Mechanical Engineering Science*, 236(23):11160-11179.
https://doi.org/10.1177/09544062221110729

Hinze JO, 1975. Turbulence. McGraw-Hill Publishing Co., New York, USA.

Huo J, Luan XY, Gong YW, Wang Z, Jiang JC and Zhang B, 2021. Numerical study of bund overtopping phenomena after a catastrophic tank failure using the axisymmetric approach. *Process Safety and Environmental Protection*, 153:464-471.
https://doi.org/10.1016/j.psep.2021.07.044

Iravani M and Toghraie D, 2020. Design a high-pressure test system to investigate the performance characteristics of ball valves in a compressible choked flow. *Measurement*, 151:107200.
https://doi.org/10.1016/j.measurement.2019.107200

Kumagai K, Ryu S, Ota M and Maeno K, 2016. Investigation of poppet valve vibration with cavitation. *International Journal of Fluid Power*, 17(1):15-24.
https://doi.org/10.1080/14399776.2015.1115648

Li BB, Zhao Q, Li HY, Liu XM, Ma JC and Fan Z, 2021. Analysis method of the cavitation vibration signals in poppet valve based on EEMD. *Advances in Mechanical Engineering*, 13(2):1687814021998114.
https://doi.org/10.1177/1687814021998114

Lu L, Zou J, Fu X, Ruan XD, Du XW, Ryu S and Ochiai M, 2009. Cavitating flow in non-circular opening spool valves with U-grooves. *Proceedings of the Institution of Mechanical Engineers Part C: Journal of Mechanical Engineering Science*, 223(10):2297-2307.
https://doi.org/10.1243/09544062JMES1504

Lu L, Xie SH, Yin YB and Ryu S, 2020. Experimental and numerical analysis on the surge instability characteristics of the vortex flow produced large vapor cavity in u-shape notch spool valve. *International Journal of Heat and Mass Transfer*, 146:118882.
https://doi.org/10.1016/j.ijheatmasstransfer.2019.118882

Lu L, Wang J, Li MR and Ryu S, 2022. Experimental and numerical analysis on vortex cavitation morphological characteristics in u-shape notch spool valve and the vortex cavitation coupled choked flow conditions. *International Journal of Heat and Mass Transfer*, 189:122707.
https://doi.org/10.1016/j.ijheatmasstransfer.2022.122707

Manninen M, Taivassalo V and Kallio S, 1996. On the mixture model for multiphase flow. Technical Report No. VTT-PUB-288, Technical Research Centre of Finland, Espoo, FI.

Martelli M, Gessi S, Massarotti GP, Marani P and Zarotti LG, 2017. On peculiar flow characteristics in hydraulic orifices. Fluid Power Systems Technology, p.V001T001A057.
https://doi.org/10.1115/FPMC2017-4313

Min W, Wang HY, Zheng Z, Wang D, Ji H and Wang YB, 2020. Visual experimental investigation on the stability of pressure regulating poppet valve. *Proceedings of the Institution of Mechanical Engineers Part C: Journal of Mechanical Engineering Science*, 234(12):2329-2348.
https://doi.org/10.1177/0954406220905872

Nicoud F and Ducros F, 1999. Subgrid-scale stress modelling based on the square of the velocity gradient tensor. *Flow, turbulence and Combustion*, 62(3):183-200.
https://doi.org/10.1023/A:1009995426001

Nourazar S and Safavi M, 2017. Two-dimensional large-eddy

simulation of density-current flow propagating up a slope. *Journal of Hydraulic Engineering*, 143(9):04017035.
https://doi.org/10.1061/(ASCE)HY.1943-7900.0001329

Pan M, Plummer A, 2018. Digital switched hydraulics. Frontiers of Mechanical Engineering, 13:225-231.
https://doi.org/10.1007/s11465-018-0509-7

Roache PJ, 1998. Verification and validation in computational science and engineering. NM: Hermosa, Albuquerque, USA.

Roohi E, Zahiri AP and Passandideh-Fard M, 2013. Numerical simulation of cavitation around a two-dimensional hydrofoil using VOF method and LES turbulence model. *Applied Mathematical Modelling*, 37(9):6469-6488.
https://doi.org/10.1016/j.apm.2012.09.002

Schnerr GH and Sauer J, 2001. Physical and numerical modeling of unsteady cavitation dynamics. Fourth international conference on multiphase flow. pp.1.

Singhal AK, Athavale MM, Li HY, Jiang Y, 2002. Mathematical basis and validation of the full cavitation model. *Journal of fluids engineering*, 124(3):617-624.
https://doi.org/10.1115/1.1486223

Stosiak M, Skačkauskas P, Towarnicki K, *et al*., 2023. Analysis of the Impact of Vibrations on a Micro-Hydraulic Valve Using a Modified Induction Algorithm. *Machines*, 11(2):184.
https://doi.org/10.3390/machines11020184

Tamburrano P, Plummer AR, Distaso E and Amirante R, 2019. A review of direct drive proportional electrohydraulic spool valves: industrial state-of-the-art and research advancements. *Journal of Dynamic Systems, Measurement, and Control*, 141(2): 020801.
https://doi.org/10.1115/1.4041063

Wang S, Zhang B, Zhong Q and Yang HY, 2017. Study on control performance of pilot high-speed switching valve. *Advances in Mechanical Engineering*, 9:1687814017708908.
https://doi.org/10.1177/1687814017708908

Yuan C, Song JC and Liu MH, 2019. Investigation of flow dynamics and governing mechanism of choked flow for cavitating jet in a poppet valve. *International Journal of Heat and Mass Transfer*, 129:113-131.
https://doi.org/10.1016/j.ijheatmasstransfer.2018.09.065

Yuan C, Song JC, Zhu LS and Liu MH, 2019. Numerical investigation on cavitating jet inside a poppet valve with special emphasis on cavitation-vortex interaction. *International Journal of Heat and Mass Transfer*, 141:1009-1024.
https://doi.org/10.1016/j.ijheatmasstransfer.2019.06.105

Yuan C, Zhu LS, Liu SQ and Li H, 2021. Examination of viscosity effect on cavitating flow inside poppet valves based on a numerical study. *Applied Sciences*, 11(23):11205.
https://doi.org/10.3390/app112311205

Yuan C, Zhu LS, Liu SQ, Du ZL and Li H, 2022. Numerical study on the cavitating flow through poppet valves concerning the influence of flow instability on cavitation dynamics. *Journal of Mechanical Science and Technology*, 36(2):761-773.
https://doi.org/10.1007/s12206-022-0124-8

Zhang JH, Wang D, Xu B, Gan MY, Pan M and Yang HY, 2018. Experimental and numerical investigation of flow forces in a seat valve using a damping sleeve with orifices. *Journal of Zhejiang University SCIENCE A*, 19(6):417-430.
https://doi.org/10.1631/jzus.A1700164

Zwart PJ, Gerber AG, Belamri T, 2004. A two-phase flow model for predicting cavitation dynamics. Fifth international conference on multiphase flow, pp.152.

Electronic supplementary materials

The momentum equations for 2D axisymmetric geometries S1
The Wall-Adapting Local Eddy Viscosity (WALE) model S2
The Schnerr-Sauer model S3
Tablet S4
GCI calculation formulas S5
Nomenclature S6

中文概要

题　目：锥阀漩涡空化几何形态变迁与流量饱和特性

作　者：陆亮 [1,2]，梁中栋 [1]，刘禹明 [1]，王志鹏 [2]，Shohei Ryu [3]

机　构：[1] 同济大学，机械与能源工程学院，中国上海，201804；[2] 同济大学，上海自主智能无人系统科学中心，中国上海，201210；[3] 日立建机株式会社，技术研究实验室，日本土浦，300-0013

目　的：伴随数字阀在流体控制中高端品质的日益体现，锥阀作为数字阀的主要阀芯结构，其空化与流量饱和问题日益受到重视。本文借助实验与仿真手段，旨在揭示漩涡空化成形机理及其伴随孔口长径比形态变迁的物理规律，以及大尺度空化对流量饱和的影响特性，为高品质锥阀结构设计提供基础依据。

创新点：1. 应用流束收缩理论定义了锥阀固定型与离散型空化的漩涡成型机理与形态变迁规律；2. 使用LES大涡模拟合理复现了空化形态并揭示了空化对流量饱和的影响规律。

方　法：1. 通过可视化实验，获得锥阀空化的几何形态，并验证数值模型的合理性；2. 通过数值计算，研究空化形态随锥阀结构的变化规律；3. 利用阀口开度、密封长度和阀芯半锥角三个参数定义长径比无量纲指标，衡量空化形态与流量饱和特性的变化规律。

结　论：1. 锥阀阀口流束内外收缩性质的不同，导致阀口

内部固定漩涡与阀口下游离散漩涡的差异，进而
形成固定漩涡空化和离散漩涡空化的形态区别；
2.使用阀口开度、密封长度和阀芯半锥角定义阀
口等效长径比，可用于评价空化几何形态的变迁
规律；3.固定漩涡空化对流量饱和的影响程度较
大，离散漩涡空化因完整的溃灭过程而对流量饱
和影响较小。

关键词：锥阀；流束收缩；漩涡流动；蒸汽空穴；流量饱
和